Electrical percolation threshold of magnetostrictive inclusions in a piezoelectric matrix under simulated sintering conditions

Antoine Joseph Bedard Jr.[1] and Ever J. Barbero[2]

ABSTRACT

Magnetoelectric (**ME**) composites can be produced by embedding magnetostrictive **H** particles in a piezoelectric **E** matrix derived from a piezoelectric powder precursor. Previously, using a bi-disperse hard shell model [1], it has been shown that the electrical percolation threshold of the conductive **H** phase can be increased by decreasing the piezoelectric **E** particle size, relative to the **H** phase particle size, and by increasing short range affinity between the **E** and **H** particles. This study builds on our previous study by exploring what happens during sintering of the **ME** composite when either the **H** or **E** particles undergo deformation. It was found that deformation of the **H** particles reduces the percolation threshold, and that deformation of **E** particles increases interphase **H-E** mechanical coupling, thus contributing to enhance **ME** coupling.

Key words: magnetostrictive, piezoelectric, magnetoelectric, particle dynamics, sintering, LAMMPS

1. Introduction and Objectives

Magnetostriction is a property of ferromagnetic materials that causes them to deform with strain when exposed to a magnetic field. The piezoelectric effect is the ability to generate electrical potential in response to an applied mechanical strain [2–7]. Magnetoelectric (**ME**) composites combine magnetostrictive **H** and piezoelectric **E** materials into a composite that can convert a magnetic field into an electric field or vise-versa with improved efficiency and sensitivity [6–8]. Previous work [2,3] describe how to maximize the **ME** effect as a function of **H** concentration, i.e. piezomagnetic volume fraction ($p=V_H/(V_H+V_E)$), where V_H, V_E are the volume of the **H** and **E** phases respectively.

[1] Assistant Professor, Sullivan University, Louisville, KY, USA
[2] Professor, West Virginia University, WV, USA. Corresponding author.
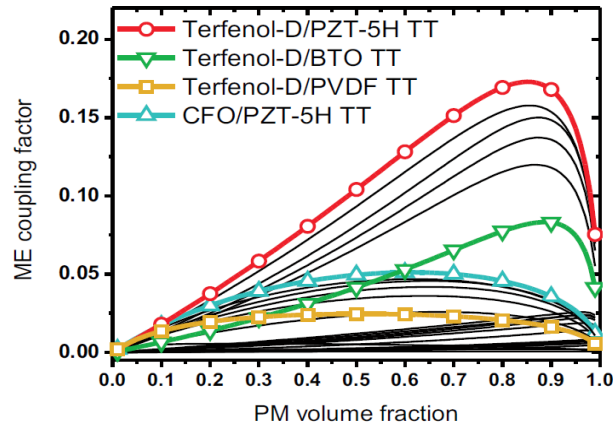
Fig. 1. Magnetoelectric coupling as a function of the relative amount of magnetostrictive material shows an optimal concentration for maximum ME coupling.

As illustrated in Fig. 1, the magnetoelectric coupling (**ME**), which measures the efficiency of energy conversion from magnetic to electric media, increases with the piezomagnetic (**PM or H**) volume fraction content. However, the **H** phase is electrically conductive and its volume fraction is limited by electrical percolation because electrical conductivity diminishes the **ME** effect. Furthermore, sintering deforms the **H** particle shape, with deformation having a deleterious effect on the electrical percolation threshold (ρ_c), and particles attaining the maximum percolation threshold when they are spherical. As per Fig. 1, one wishes to maximize the percolation threshold so that a larger volume of **H** phase can be used in order to maximize **ME** coupling.

Sintering is a process by which powders are densified to remove interstitial space so that the packing fraction approaches one and bonds are formed between precursor particles. Sintering is done at temperatures generally below the composite melting temperature [9,10]. Numerical techniques have been employed to study the sintering of close packed spheres [11], and numerous experimental studies have been conducted to investigate the sintering of magnetostrictive and piezoelectric ceramic composites [12–14], which report the use of conventional ceramic processes by applying pressure with a chemical binder that promotes bonding to produce a pellet followed by applying heat below the precursor's melting

temperature but sufficient to evaporate the binder. Another method reported for sintering ceramics is electric current assisted sintering (ECAS), where powders are inserted into a container that is heated by applying electric current through the powders while pressure is applied at a fixed temperature for a given period of time [15]. In yet another method, magnetoelectric PZT-CFO is produced via a chemically driven ethlenediaminetetraacetic acid (EDTA)-citrate gel process [16]. In all cases, deformation of the constituent particles occurs as a result of pressure and high temperatures or the transport of matter by viscous flow, evaporation, or atomic volume and surface migration [10,17,18]. Consequently, any process considering electrical conduction among particles in a composite must consider the relative shape of those particles, which may form a conductive chain in the composite manufacturing process.

Aiming to exploit the as of yet unrealized **ME** optimization per Fig. 1 [2,3], and using a hard shell model, [1] explored the relationships between particle size, inter-phase affinity and particle attraction, and the electrical percolation threshold [19,20] in the electrical conducting magnetostrictive (**H** phase) when mixed with the nonconductive piezoelectric (**E** phase) for the purpose of maximizing the magnetoelectric (**ME**) effect. Barbero and Bedard [1] concluded that the electrical percolation threshold increases when size of the **E** piezoelectric particles is reduced, and also when short range attractive or adhesive quality is introduced between the **H** and **E** phases. However, these results [1] were predicated on the assumption that neither the **H** nor **E** particles deformed from their idealized state of hard solid spheres but either or both **H** and **E** particles may deform during sintering. Therefore, the objective of this study is to address the effect of particle deformation on the electrical percolation threshold of the **H** phase. Furthermore, it is also the objective of this study to investigate, through simulation, the likely effect of particle deformation on mechanical contact between both phases, which is needed to effectively transfer the strains from the piezomagnetic **H** phase to the piezoelectric **E** phase, which is crucial for achieving a high performance device [21].

2. Methodology

To simulate mesoscale (100 nm) particle interactions particle dynamics is performed using Large Scale Atomic and Molecular Massively Parallel Simulation LAMMPS software [22]. All interactions between particles are modeled with the well-known Lennard-Jones potential, and all results are expressed in Lennard-Jones natural units of ε and σ for energy and distance respectively.

2.1 Simulation Specifications

The simulation box initially contains 8000 spherical particles each a diameter of 1.12246σ. A fraction $p = N_H/(N_H + N_E)$ of the particles are coded **H** for magnetostrictive while the rest a coded **E** for piezoelectric, where N denotes number of particles. Per [1], initially the hard-shell simulation contains only particle modeled as spheres and is run in three stages to allow the particles to be mixed, but also rendered at a final packing fraction $f = 0.64$, which is the density at which random close packed particles jam or undergo a glass transition [23–25]. The first stage is the mixing (MIX) stage where particles are mixed at a low packing fraction of $f = 0.5236$ corresponding to the crystalline simple cubic lattice to allow sufficient space for complete mixing. In the second stage, referred to as equilibration (EQU), the particle size is scaled up (by increasing σ in the Lennard-Jones potential) to increase the packing fraction to an intermediate value where the particles are allowed to equilibrate and relax the potential energy that increased as a result of the increased particle size [1]. In the third or gelation (GEL) stage, the particles are again grown so that the packing fraction reaches the jamming [23] or glass transition [24,25] value of $f = 0.64$.

After the three stages MIX, EQU, and GEL are completed, the **H** particles are replaced with deformable cubes with each cube containing 125 smaller spheres (Fig. 3), and where each smaller sphere is modeled with a Lennard-Jones sigma value of $1.22246/5$ or 0.22492σ. See Appendix C regarding LAMMPS© input scripts for details. Post processing calculations for computing the coordination numbers (**c.n.**) and radii of gyration (**R$_g$**) are performed with programs written in PERL and C per Appendices A and B. The algorithms **dist9M.c** and **zapM.c** are developed and used to measure percolation between deformed **H** clusters. The same recursive algorithm referred to as **zap2.c**, previously

used to measure hard-sphere percolation in [1] is here modified to compute the smallest distance between all possible contact points between clusters. See Appendices for details.

3. Two Dimensional Particles Dynamics

Although this study involves full three dimensional simulation, the results of two dimensional simulations are easier to visualize, thus two dimensional simulations are initially performed to see if particle clusters diffuse around larger spherical particles in a way that mimics particle deformation that occurs during actual sintering. Fig. 2 illustrates that **H** clusters deform and diffuse in a way supporting the goals of this study, which is to explore the effect of sintering on the percolation threshold and inter-phase mechanical contact [1]. In Fig. 2, it can be seen that after some time, the colored circles (**H** phase clusters) deform and fill the interstitial spaces between the hard blue spheres (**E** phase). This is accomplished by slowly growing all particles in both phases in small discrete steps at the same rate until the interstitial spaces are filled and the packing fraction ($f=V_H+V_E/V_{box}$) approaches one, which is a primary objective of the sintering process. V_H, V_E, and V_{box} refer to the volume of the **H** phase, **E** phase, and simulation box respectively.
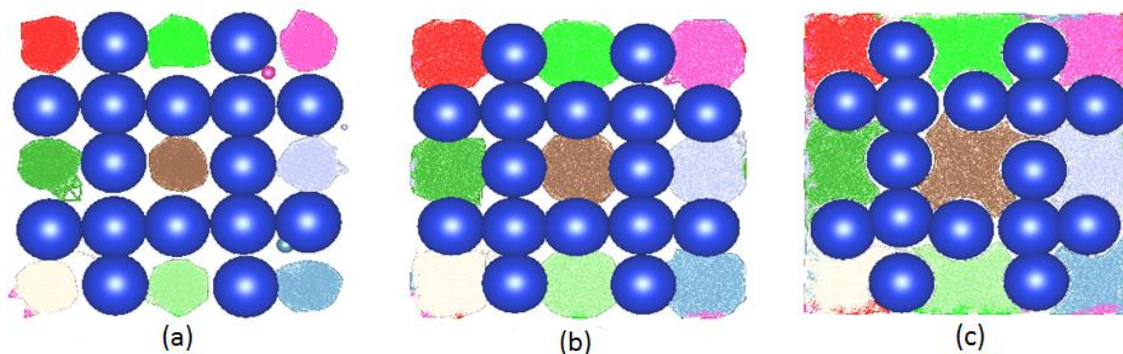

(a) (b) (c)

Fig. 2. 2D simulation with H-clusters deforming around undeformable spherical E-particles

4. Three Dimensional Particle Dynamics

This study involves two parts. The first part is to simulate the mixing of magnetostrictive **H** and piezoelectric **E** powders where the **H** clusters are modeled as small cubes, each composed of 125 small spheres per cube (Fig. 3). Each small sphere in a **H** cluster is modeled using the Lennard-Jones "6-12"

potential. All **E** particles are also modeled as hard-shell spheres using the Lennard-Jones "6-12" potential with modeling parameters adjusted to reflect larger size and interaction energy well depth. The particles within each cube are allowed to move for a short time (Section 4.1) until the spheres are in a random configuration but still close enough to each other to constitute a cluster as shown in Fig. 4. Once the dense but random configuration of small spheres as shown in Fig. 4 is achieved, the motion is stopped (Sect. 4.1), and the collection of smaller spheres, referred to as clusters are regarded as equivalent to a continuous matter distribution of equal proportions (Fig. 5).
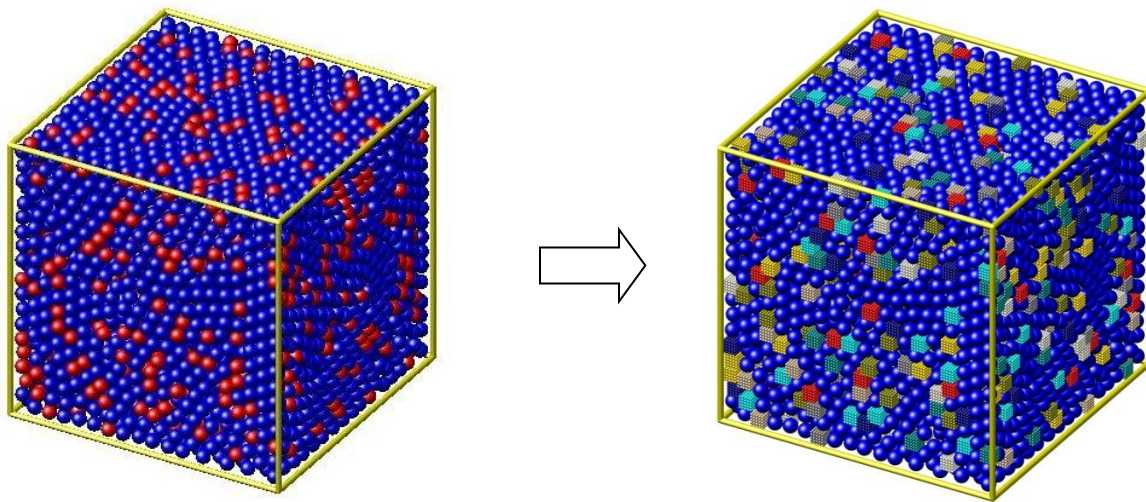

Fig. 3. Left: Hard-sphere result from [1] state GEL, No affinity (Noa). Right: All H-phase red spheres on left replaced with 125 point cluster cubes.
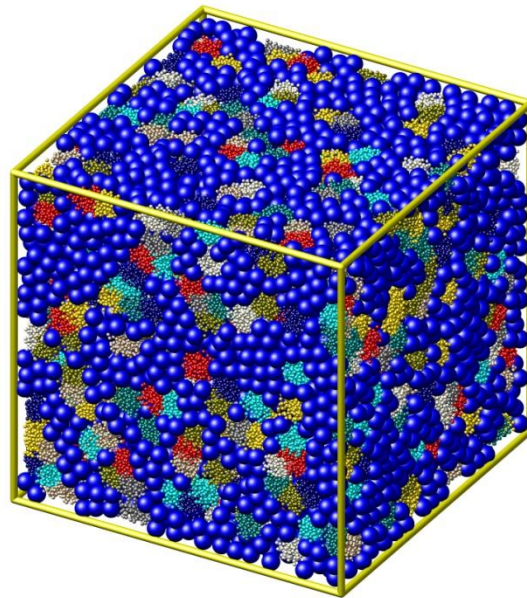
Fig. 4. **H** clusters deform and diffuse to fill the interstitial space between **E** phase spheres.
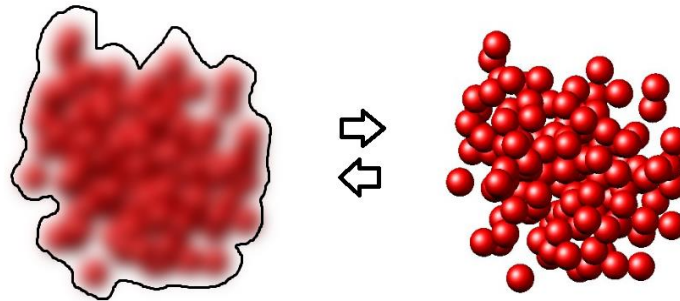

Fig. 5. Continuum of matter is replaced by 125 discrete particles in a cluster.

4.1 Stopping Time

During actual sintering, particle shape changes due to diffusion and surface migration, and this change stops when the local gradient of the chemical potential between diffusing species becomes exhausted [9,10,26]. In addition, in actual sintering, mass transport involving phase change mostly occurs over small distances relative to particle size in a compacted powder mix [9], so we restrict particle migration to local movement only. However, in the present simulation and taking into account that the Lennard-Jones potential represents a frictionless elastic potential, mass transport would never stop unless a dampening or a reduction in temperature are introduced. Therefore, in this study, to avoid excessive

mass transport, an end-of-simulation condition is chosen to restrict the amount of medium and long range matter transport to under approximately 25% of all matter in any given cluster.

In order for the clusters to simulate a continuous mass, the spheres in each cluster must be relatively close to each other. If any sphere in a cluster exceeds a distance greater than $2 \times \mathbf{R_g}$ ($\mathbf{R_g}$ = Radius of Gyration, see Section 5.2) from that cluster's center of mass (Fig. 6), then those small spheres are not counted as part of the continuous distribution for the purposes of computing percolation, but are still used to compute the coordination number **c.n.** (Section 5.3). It can be seen in Table 3 that on the average the percent of small spheres outside $2 \times \mathbf{R_g}$ are less than 25% for a simulation time of 3800 time steps, with an iterative time step coded into LAMMPS [22] of $\Delta t = 0.0002$.

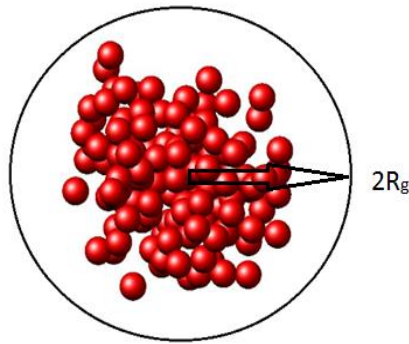**Fig. 6.** Particles at a distance greater than $2 \times \mathbf{R_g}$ from cluster center of mass excluded from electrical percolation calculations.

4.2 Range Calculations

A key parameter needed to compute both the intra-phase **H-H** percolation and the **H-H** or **H-E** coordination numbers is the maximum range $\mathbf{R_m}$ (in distance units of $\boldsymbol{\sigma}$) allowed between the centers of two particles such that the particles are considered connected. There are three distinct situations for calculating range. The first (Fig. 7a) is the electrical contact distance between **H** hard-shell spheres given by equation (1) where **D** is the diameter of **H** phase sphere=1.12246σ, SF is scaling factor=$(f/0.5236)^{1/3}$ (Section 4.2.1) and QT is factor to account quantum tunneling=$(1+5/100)=1.05$ per section 4.2.2.

Quantum tunneling is based upon particle size and is scaled to 100 nm corresponding to 5nm electrical quantum tunneling distance [27–29]. Quantum tunneling considers the effect that classically isolated conducting particles may still be electronically connected due to the wave nature of charge carriers [28,29]. The scaling factor (SF) is a factor applied to sigma (σ) in the Lennard-Jones inter-particle potential to maintain the packing fraction at the random close packed critical values of f=0.64,0.675,0.73, 0.755, which are the particle densities above which jamming or glass transition occurs and motion becomes arrested for R_H/R_E = 1,2,3,4 respectively [30,31] (Section 4.2.1).

The second range (Fig. 7b) computed via equation (2) is the mechanical contact between any small spheres in an **H** cluster and a nearby **E** particle. For this mechanical contact range, no quantum tunneling is involved and the distance between the particles centers is 3/5 the diameter of an **E** particle.

The third range is given by equation (3) and is the electrical contact distance between deformed **H**-clusters. In this third case the distance between the effective surfaces of two **H** clusters is D×QT-D (Fig. 7c), and the additional distance between the centers of 2 smaller spheres within each cluster is D/5. Thus, the total effective electrical distance is SF×[D×QT-D + D/5] scaled up, where quantum tunneling (QT) is the additional distance an electrical signal may travel between classically isolated conducting particles [1], and the scaling factor (SF) is applied to all particles both **E** and **H** to maintain the packing fraction at f=0.64 in the case where R_H/R_E=1. Table 1 displays the range calculations used in this study per equations 1-3.

4.2.1 Derivation of scaling factor SF

Particles are sized to allow a packing fraction **f** that allows adequate room for mixing below glass transition or jamming, i.e. motion restriction [23,24]. After mixing, all particles are scaled up in size to rescale the simulation to the packing fraction below which we hypothesis adequate sintering would not occur efficiently because the particles would not be compacted. Let r_1 be the particle radius before scaling and r_2 be the particle radius after scaling. For equally sized particles (R_H/R_E=1), to increase the packing fraction to f =0 .64 for a fixed box volume V_{box}, r_1 must be increased such that $(4/3)\,\pi\,(r_2)^3 / (4/3)$

$\pi\,(r_1)^3 = 0.64/0.5236$. This means that $r_2 = (0.64/0.5236)^{1/3} \times r_1 = SF \times r_1$. Therefore, the scaling factor

(SF) for $R_H/R_E=1$ is calculated as $SF = (0.64/0.5236)^{1/3} = 1.069203$. In general for all SF values listed in

Table 1, $SF = (f/0.5236)^{1/3}$ where f is the associated packing fraction for that particles size.

4.2.2 Quantum tunneling

Quantum tunneling is an effect whereby electric charge can jump a space between conductive but

electrically isolated particles that is forbidden by classical mechanics [28].   Quantum tunneling is

reported to range from 3 nm [28] to 10 nm [32] between conducting particles in a non-conducting matrix.

Per [1], if two conducting particles are at most 5 nm or closer, then there is a high likelihood of quantum

tunneling between the two conducting particles of diameter 100 nm, so when the **H** particle diameter

D=100 nm, the conductivity distance used to evaluate percolation between particles centers is increased

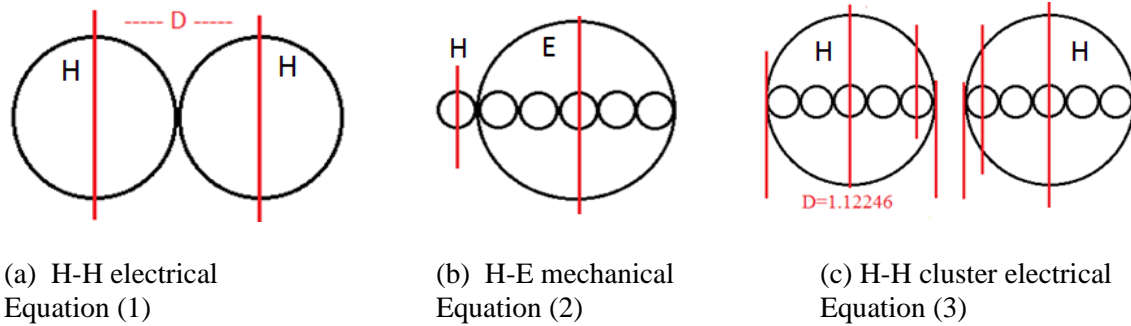by a factor of $(100 + 5/100) = 1.05$.

(a) H-H electrical   (b) H-E mechanical   (c) H-H cluster electrical
Equation (1)   Equation (2)   Equation (3)

Fig. 7. Illustrations for range calculations given by equations 1-3.

$$R_m = D \times GF \times QT \quad (1)$$

$$R_m = 3 \times \frac{D}{5} \times GF \quad (2)$$

$$R_m = GF \times \left(D \times QT - D + \frac{D}{5}\right) = GF \times \frac{D}{4} \quad (3)$$

Table 1. Range calculations per equations 1-3 and R_H/R_E= 1-4, **f** = packing fraction (sect. 5.1), **SF** = scaling factor (sect. 4.2.1), **QT** = quantum tunneling (sect. 4.2.2), **R_m** = range (sect. 4.2, equations 1-3)

parameter	f	SF	QT	R_m
c.n.$_{H-H}$ (R_H/R_E=1)	0.64	1.0692	1.05	1.26
c.n.$_{H-E}$ (R_H/R_E=1)	0.64	1.0692	1	1.2
c.n.$_{H-E}$(R_H/R_E=2)	0.675	1.08835	1	0.92
c.n.$_{H-E}$(R_H/R_E=3)	0.73	1.11714	1	0.84
c.n.$_{H-E}$(R_H/R_E=4)	0.755	1.12975	1	0.79
c.n.$_{H-E}$ (cluster)	0.64	1.0692	1	0.72
c.n.$_{H-H}$ (cluster)	0.64	1.0692	1.05	0.25
perc. dist. ρ_c (R_H/R_E=1)	0.64	1.0692	1.05	1.26
perc. dist. ρ_c (R_H/R_E=2)	0.675	1.08835	1.05	1.28
perc. dist. ρ_c (R_H/R_E=3)	0.73	1.11714	1.05	1.32
perc. dist. ρ_c (R_H/R_E=4)	0.755	1.12975	1.05	1.33
perc. dist. ρ_c (clusters)	0.64	1.0692	1.05	0.3

4.3 Process and Thermodynamics

All simulations of deformable phases in this study begin with **H** and **E** particles located in space as per configuration in the GEL stage of hard-shell simulations performed in [1]. One such initial configuration of **H** and **E** particles is shown on the left of Fig. 3. Next, the **H** hard spheres are replaced with cubical clusters each containing 125 smaller Lennard-Jones spheres.

It was found initially that replacing spheres with deformable cubes at the locations occupied by the precursor hard-shell **H** spheres resulted in simulation failure because portions of the cubes invaded the **E** hard-shell boundaries, causing excessive potential energy above the legal bounds for the LAMMPS simulation software [22]. To solve this problem, the small spheres making up the deformable cubes were reduced in size until the cubes have time to deform into appropriate spherical clusters. The small spheres were then allowed to equilibrate for a short period of time, and then they were slightly scaled up in size by increasing the Lennard-Jones distance parameter **σ** and adjusting the energy parameter **ε**. The system was then allowed to equilibrate. This process of sudden but incremental scaling followed by short time equilibration was repeated until all particles were at the required size to restore the packing fraction (f = V_E+V_H/V_{box}) and volume ratio p=$V_H/(V_E+V_H)$ to the same values they had before the **H** particles were replaced with deformable cubes, where V_H and V_E equal the total volume taken up by the H and E phases respectively [1]. An example of the thermodynamics that occurs during the simulation of sintering is

shown in Fig. 8.   The potential energy (**PE**) appears discontinuous because at each discontinuity, the size of all particles both **H** and **E** are increased suddenly.   This increase in **PE** causes a corresponding increase in kinetic energy (**KE**) as shown Fig. 8.
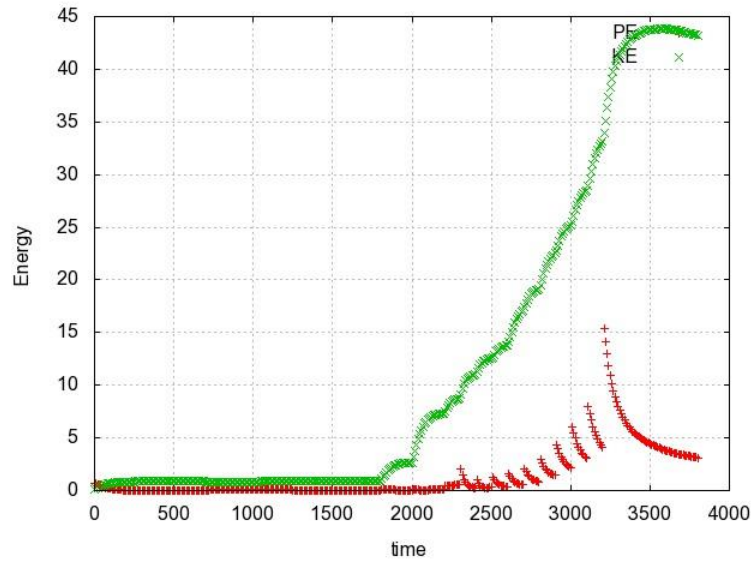

Fig. 8. "×" is Kinetic Energy   "+" is Potential Energy

5. Characterizations and Measurement

The techniques used for characterization and measurement are described in this section.

5.1 Packing fraction

The packing fraction is the volume of all solid matter relative to the volume of the simulation box and is defined per equation (4).

$$f = \frac{V_E + V_H}{V_{box}} \quad (4)$$

The volume ratio is defined per equation (5).

$$\rho = \frac{V_H}{V_{box}} = f \times p \quad (5)$$

The volume fraction is defined per equation (6).

$$p = \frac{V_H}{V_H + V_E} \quad (6)$$

5.2 Radius of Gyration

The radius of Gyration (R_g) is the distance representing the effective angular momentum of a distribution of point masses about the distribution's center of mass given by equation (7) [33]

$$R_g = \sqrt{\frac{1}{n}\sum_{i=1}^{n}(r_i - r_{cm})^2} \quad (7)$$

In this study, the radius of gyration is used to represent the three dimensional shape and deformation of the clusters. By way of comparison, the radius of gyration of **H** and **E** spheres with diameter $2 \times R = 1.12246\sigma$ is $R_g = 0.775 \times R = 0.435\sigma$, where σ is the Lennard-Jones natural unit of distance, and the R_g of a perfect sphere of this same radius is $0.775 \times 0.56123 = 0.435\sigma$. A cylinder of radius R and equal volume to an **E** or **H** sphere has a radius of gyration such that $(R_g)^2 = R^2/2 + (4/3R)^2/12$, so that $R_g = 0.452\sigma$. It can be seen that the R_g of a cylinder is larger than the R_g of a sphere of the same volume. Thus, R_g provides an indication of a cluster's deformation during sintering.

5.3 Coordination Number

The coordination number (**c.n.**) [34–38] is the average number of contacts with other particles any given particles has. In crystallography [35], the lattice structure of a simple cubic lattice has a **c.n.** = 6, a body centered cubic lattice has a **c.n.** = 8, and the hexagonal closest packed has **c.n.** = 12. In this study, we define two types of coordination numbers. The first, CNHH (left Fig. 9), is the number of contacts the average **H** particle make with other **H** particles, which is important for electrical conduction. The other type of coordination number, labeled CNHE (right Fig. 9), is the number of contacts the average **H** particle makes with other **E** particles, which is important for mechanical contact and deformation transfer between phases.

Fig. 9. Illustration for coordination numbers intra-phase CNHH (left), and inter-phase CNHE (right)

Per Fig. 9, CNHH characterizes the percolation paths an electrical signal could follow. Thus the higher the CNHH, the more likely the percolation threshold (ρ_c) is to decrease. CNHE characterizes the mechanical contact between the **H** and **E** phases, which is proportionate to the efficiency of energy transfer between the **H** and **E** phases. All small spheres belonging to a particular cluster may participate in the calculation for either coordination number regardless of distanced from center of mass. The average **c.n.** for random close packed configurations of perfect spheres of equal size is reported to be approximately six [34,37]. Higher CNHH and CNHE values provide an indication of a lower percolation threshold or higher **ME** electromechanical contact, respectively.

6. Results

6.1 Deformation of **H** Phase around Rigid **E** Phase

This section addresses what happens when the **H** particles deform around rigid **E** particles. In Table 2, "RU" in the left most column stands for the initial configuration of particles used in this study taken from after the GEL stage completed in [1]. "Noa" stands for "No affinity" between any particles used to compute the initial configuration under GEL conditions per [1]. "Adh" stands for "Affinity" between **H** and **E** phase particles used to compute the initial configuration under GEL conditions per [1]. "ρ_c" represents the critical or smallest volume ratio, $\rho=V_H/(V_{box})$ where electrical H-H percolation occurs. V_H is the volume of the H phase and V_{box} is the total volume of the simulation box for this study which is $(20\times1.12246\sigma)^3$. R_g is the radius of gyration in Lennard-Jones units of sigma σ.

Furthermore in Tables 2 and 3, "Bonds" stands for the number of bonds between deformed H particles found during percolation.   "CNHH" stands for the coordination number of all **H** particles with respect to other **H** particles when all particles are modeled as hard-shell spheres with $R_H/R_E=1$ that is data from [1]. CNHE1 through CNHE4 stands for the coordination number of all **H** particles with respect to surrounding **E** particles for $R_H/R_E = 1,2,3,4$ respectively.   We see in Table 2 that the sum of CNHH and CNHE1 is approximately six which corresponds to the average coordination number of random close packed spheres of equal size [34,36,37]. Also in Table 2, it can also be seen that for the no inter-particle (Noa) cases, the inter-phase **H-H** coordination CNHH tracks in direct proportion with the percolation

threshold ρ_c. That is, as the **H-H c.n.** goes up or down, so does the **H-H** electrical percolation threshold.

Also, it can be seen that the inter-phase particle coordination numbers CNHE1 to CNHE4 increase

sharply with increasing difference in particle size $R_H/R_E = 1$ to 4. See Fig. 13 for additional information

regarding this trend.

Table 2. Characterization of hard-shell spheres simulation

	ρ_c	Rg	Bonds	CNHH	CNHE1	CNHE2	CNHE3	CNHE4
RU8/Noa	0.25	0.435	1802	2.07	3.84	17.74	39.18	59.11
RU9/Noa	0.26	0.435	1450	2.21	4.19	17.16	38.8	56.37
RU10/Noa	0.22	0.435	1245	1.74	4.45	18.36	44.72	60.75
AVG	0.243	0.435	1499.000	2.007	4.160	17.753	40.900	58.743
STD	0.021	0.000	281.714	0.241	0.306	0.600	3.314	2.213
COV	8.555	0.000	18.793	12.026	7.358	3.380	8.102	3.767
RU8/Adh	0.3	0.435	1653	1.68	4.77	18.01	39.44	60.82
RU9/Adh	0.3	0.435	1931	1.73	4.86	19.33	39.29	59.72
RU10/Adh	0.29	0.435	1626	1.63	4.88	18.3	40.27	58.59
AVG	0.297	0.435	1736.667	1.680	4.837	18.547	39.667	59.710
STD	0.006	0.000	168.838	0.050	0.059	0.694	0.528	1.115
COV	1.946	0.000	9.722	2.976	1.211	3.740	1.331	1.867

The effects of **H** particle deformation are reported in Table 3. "A00/#" stands for no affinity between

any particles, and "A12/#" stands for affinity between the **H** and **E** phase during the additional 3800 time

steps used to model particle deformation, but no **H-H** or **E-E** affinities, where # stands for run number.

All runs were repeated three times.   The term "%strys" stands for the percent of small spheres per cluster

that have drifted away more than $2 \times R_g$ from the center of mass of a given cluster. "CNHH-M" stands for

the average coordination number of all **H** clusters with respect to other **H** clusters. "CNHE-M" stands for

the average coordination number of all **H** clusters with respect to all neighboring **E** particles.

Table 3. Characterization of deformable H-clusters in simulation

Noa	ρ_c	Rg	Bonds	%strys	CNHH-M	CNHE-M
A00/1	0.14	0.594	716	22.05	8.91	15.41
A12/1	0.14	0.597	715	19.29	8.81	17.72
A00/2	0.17	0.59	986	25.15	9.59	16.42
A12/2	0.17	0.593	990	22.52	9.53	19.02
A00/3	0.13	0.593	512	20.77	9.18	14.03
A12/3	0.11	0.595	281	18.3	9.52	15.63
AVG	0.143	0.594	700.000	21.347	9.257	16.372
STD	0.023	0.002	274.693	2.457	0.341	1.777
COV	16.312	0.394	39.242	11.509	3.682	10.855

Adh	ρ	Rg	Bonds	%strys	CNHH-M	CNHE-M
A00/1	0.15	0.588	792	24.75	8.28	16.55
A12/1	0.15	0.592	719	15.54	8.16	18.32
A00/2	0.17	0.59	986	25.15	9.59	16.42
A12/2	0.17	0.593	990	25.52	9.53	19.02
A00/3	0.14	0.589	754	15.54	8.6	15.42
A12/3	0.14	0.592	755	12.68	8.49	17.21
AVG	0.153	0.591	832.667	19.863	8.775	17.157
STD	0.014	0.002	122.523	5.879	0.628	1.323
COV	8.910	0.333	14.715	29.597	7.152	7.713

It can be seen in Table 3 that the percolation threshold based on "**H-E** particle affinity (Adh)" initial conditions (Table 3, bottom half) is higher than percolation threshold derived from "no affinity (NOA)" initial conditions. This reinforces the conclusion that **H-E** particle affinity increases the **H-H** percolation

threshold regardless of **H** particle deformation. It may be seen that both the CNHH-M and CNHE-M

values have a relatively low spread about their average values, and that the "A00" (No particle affinity

during deformation) coordination numbers are close to the "A12" (**H-E** affinity during sintering)

coordination numbers, while the R_g values are almost the same in all cases.   This indicates that when

particle deformation is used as the stopping condition (section 3.1), the percolation threshold is relatively

independent of how the particles reached their final geometrical state, i.e. particle clusters are independent

of path taken in phase-space to arrive at their asymmetrical conformations in space, assuming no phase

transition were crossed.

   A comparison between the results of Tables 2 and 3 is presented in Table 4 where average values and

their associated coefficients of variance (COV) from Tables 2 and 3 are reported. It can be seen in Table

4 that regardless of whether the **H** phase deformation is started from the hard-shell adhesive (Adh) or

non-adhesive (Noa) hard-shell configurations [1], the percolation threshold (ρ_c) drops from 0.243 to 0.143

(Noa conditions), or from 0.297 to 0.153 (Adh conditions) as the radius of gyration (R_g) increases from a

value associated with perfectly spherical ($R_g = 0.435\sigma$) to values of R_g between 0.591σ to 0.594σ

associated with clusters of small asymmetrical spheroids (Fig. 10).

   In Fig. 11 a representative histogram of R_g values is shown for a case of no affinity (Noa) during

placement of particles as they are at completion of the hard-shell GEL stage [1], followed by no affinity

(A00) simulation conditions during time evolution of the deformable clusters for this study.

Table 4. Comparison of Tables 2 and 3.

Noa	No sintering Hard-shell	Pseudo-sintering Deformation	Comments
ρ_c	0.243 (8.55) →	0.143 (16.31)	Perc. threshold decreases
R_g	0.435 →	0.594 (0.394)	Sphere deforms
CN_{H-H}	2.01 (12.03) →	9.26 (3.68)	Gain mechanical contact
CN_{H-E}	4.16 (7.36) →	16.37 (10.86)	Gain mechanical contact
c.n.	6.17 →	25.63	
%strys		21.35 (11.51)	

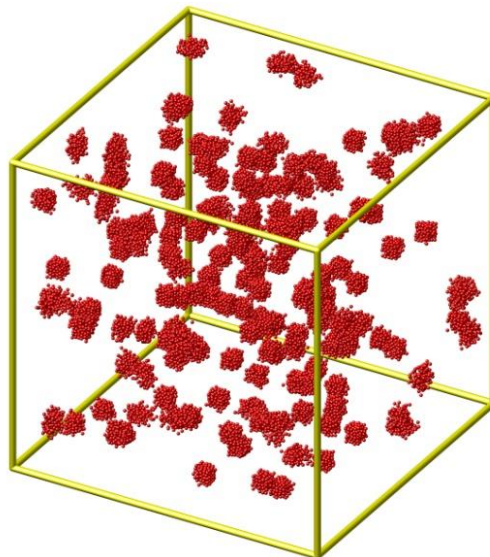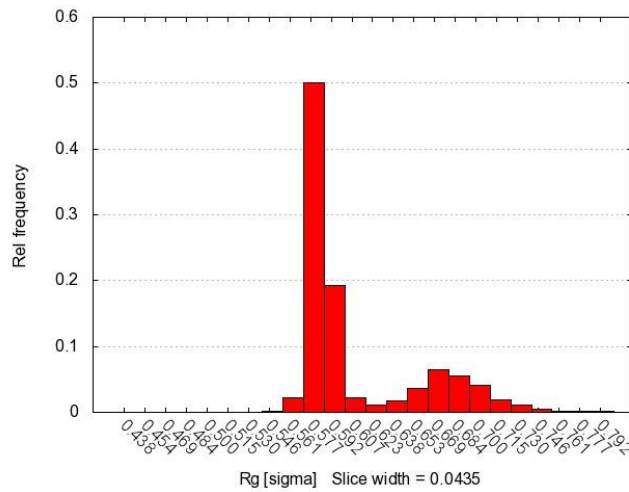| Adh	No sintering Hard-shell	Pseudo-sintering Deformation	Comments
ρ_c	0.297 (1.95) →	0.153 (8.91)	Perc. threshold decreases
R_g	0.435 →	0.591 (0.33)	Sphere deforms
CN_{H-H}	1.68 (2.98) →	8.78 (7.15)	Gain mechanical contact
CN_{H-E}	4.94 (1.21) →	17.16 (7.71)	Gain mechanical contact
c.n.	6.62 →	25.94	
%strys		19.83 (29.60)	

Fig. 10. Cube clusters morph into spheroids.

Fig. 11. Histogram of radius of gyration (R_g) under Noa followed by A00 conditions as a function of cluster deformation represented by its R_g.

Per Table 4, it can be seen that the **H** phase coordination number CNHH has values between 6 and 7, in approximate agreement with previous studies about coordination of random close packed spheres [34,36,37]. Also per Table 4, when **H** phase particle deformation is allowed, **H-H** coordination increases from a value less than 2 (CNHH hard-shell model) to values in the range 8 to 9 (CNHH-M clusters model). This indicates that the number of paths for electrical signal across the **H** phase has increased dramatically, and this increase in electrical percolation paths explains the reduction of the **H-H** electrical percolation reported in Table 4, column 2. It appears even mild deformation of the conductive **H** phase from spherical particles causes a large drop in the percolation threshold (ρ_c). Also per Table 4, CNHE (**c.n.** between the **H** and **E** phases) increases from approximately 4 to values in the range 16 to 17. This indicates that at least a fourfold increase in mechanical contact between the **H** and **E** phases has occurred while the **H** particles are mildly deformed. This is an encouraging finding as the optimum **ME** composite would be one that maximizes the **H-E** mechanical contact while minimizing **H-H** electrical percolation. In fact, for a continuous particle distribution during a physical experiment, the mechanical contact would generally be expected to increase by several orders of magnitude.

6.2 Deformation of **E** Phase around Rigid **H** Phase

This section addresses what happens if the **E** particles deform around rigid, spherical **H** spheres. The Scher-Zallen [39] invariant percolation threshold for a conducting phase (**H**) of spheres immersed in equally sized insulating (**E**) spheres is $\rho = 0.154$. Barbero and Bedard [1] found that decreasing the size of the **E** phase until $R_H/R_E=4$ could increase the percolation threshold to $\rho_c = 0.297$ or 0.243 depending on whether **H-E** particle affinity (Adh) is considered or not, respectively. In other words, the highest percolation threshold was found to be at 29.7% volume fraction of **H** phase. Therefore, the **E** phase constitutes the majority of the **ME** composite's volume, and the **E** particles are much smaller than the **H** particles ($R_H/R_E=4$). Thus, for modeling deformation of the **E** phase, it is not necessary to collect the **E** particles into small clusters. Specifically, we assume that immersing larger spherical **H** particles in a random close packed continuum of smaller **E** particles is equivalent to deforming **E** particles to fill the interstitial space between rigid **H** particles. That means that simulation with **H** and **E** hard-shell spheres using the methodology presented in [1] is able to reveal the effects of deformation of the **E** phase, as depicted, for example in Fig. 12.

Increase of percolation threshold ρ_c with decreasing size of **E** particles is apparent in Fig. 12. However, somewhere between $R_H/R_E = 3$ to 4, the percolation threshold tapers off for the case of no affinity (Noa) between the **H** and **E** phases, and it decreases or dips for the case where the **H** and **E** phases experience short range affinity (Adh). In light of this dip, we postulate that the increase in the percolation threshold (ρ_c) is due to the smaller particles moving to interstitial space between the **H** particles and hence separating the **H** particles away from each other.   However, when the **E** phase particles become too small, they can no longer push the **H** particles apart. In addition, the dip in the linear relationship between ρ_c and R_H/R_E between 3 and 4 seen in Fig. 12 becomes more pronounced when there is **H-E** affinity (Adh) between **H** and **E** particles. This is because when two large **H** particles are both attracted to the same **E** particle, they are effectively attracted to each other, decreasing the distance between **H** phase particles, and thus decreasing the percolation threshold.

The pair-wise Lennard-Jones potential used in this model does not have any friction or lateral force components, so this dip in the trend of increasing percolation threshold (ρ_c) versus R_H/R_E=1,2,3,4 shown in Fig. 12 may not be so severe in practice because actual particles will experience frictional forces that keep them from being pushed out of the way.   In the case where there is **H-E** particle affinity (Adh), because the L-J potential does not have any lateral force components, the **E** particles in this simulation can be pushed into interstitial spaces between **H** particles and act as attractors within the **H** phase, closing the distances between **H** particles and lowering the percolation threshold.
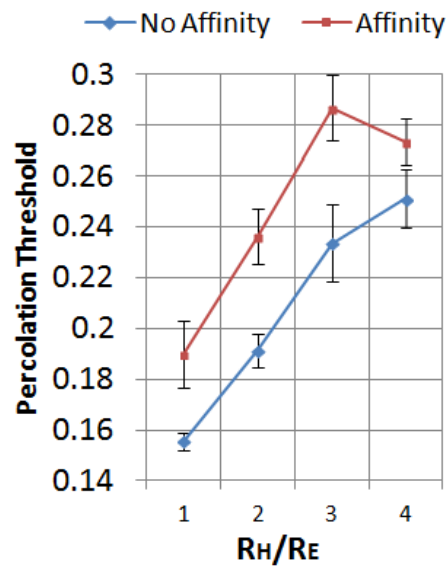

Fig. 12. Percolation threshold when both H and E phases are modeled as hard-shell spheres.
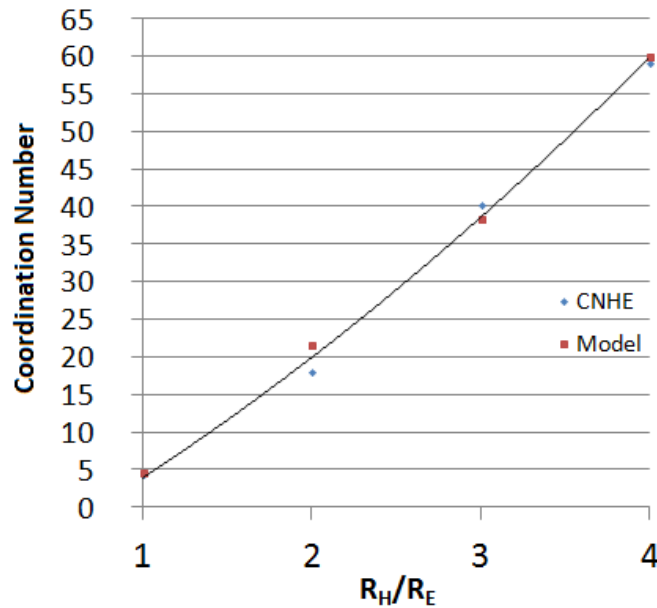
Fig. 13. CNHE1-4 H-E inter-phase coordination number of hard-shell model.

As previously mentioned, the coordination number **c.n**. is an indicator of mechanical contact because the higher the **c.n**., the larger the numbers of contacts between particles and thus the more efficient the energy transfer is. The predicted relationship between interphase **ME** mechanical contact (CNHE) and relative particle size R_H/R_E is shown in Fig. 13. When the relative size of the **E** particles decreases with respect to the **H** particles the number of bonds between the **E** and **H** particles (CNHE) increases quadratically. We propose a simple qualitative parametric model (Fig. 14) that purports that mechanical contact between **H** and **E** particles is of the same order of magnitude as the ratio of the surface area of a larger sphere centered at the **H** particle intersecting the cross sectional area of the smaller **E** particles at the **E** particle's center. This simple models results in the following equation:
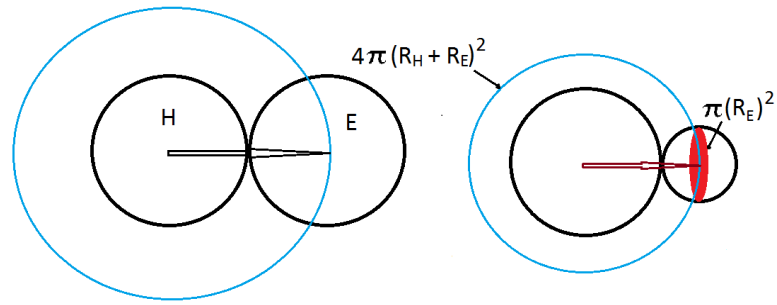
Fig. 14. Two equal size particles in contact (left), and two unequal sized particles in contact (right).

$$c.n. \propto 4\pi \frac{\left(\frac{D}{2}+\frac{D}{2x}\right)^2}{\pi\left(\frac{D}{2x}\right)^2} = 4(x+1)^2 \approx 2.4 \times \left(R_H/R_E + 1\right)^2 - 5 \qquad (8)$$

where **D** is the diameter of the **H** particles and $x = R_H/R_E$ is the ratio of the **H** to **E** particle radii. Fig. 14 illustrates the derivation of (8) where the **c.n.** × intersect area of the small sphere = the area of the larger sphere at distance R_H+R_E.
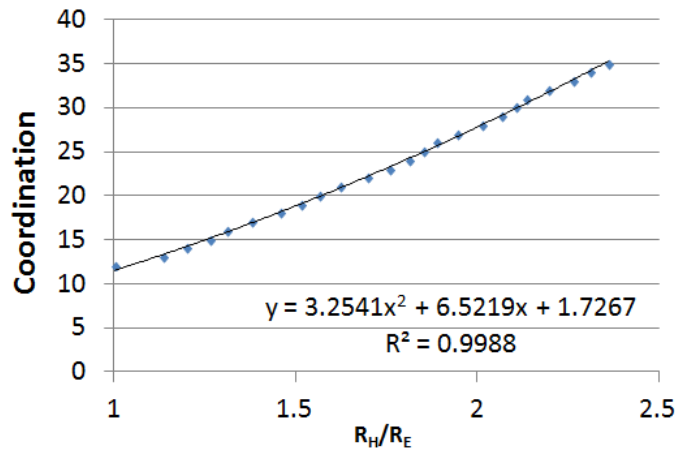

Fig. 15. Polynomial curve fit of [44] Table 2.

Liang ([40] Table 2) produced a table of coordination numbers for a bi-disperse population of spheres as a function of relative particle size. Curve fitting their results of coordination versus relative particle size shows a good fit for a quadratic polynomial (Fig. 15) thus supporting the simple model proposed in (8) representing the results of this study in Fig. 13.

7. Conclusions

In conclusion, we observed that the deformation of the electrically conducting, magnetostrictive **H** phase particles that occurs in practice due to sintering is likely to lower the percolation threshold in bi-disperse **ME** composites because the deformed particles will have more contact points and higher coordination number. Hence, any electric signal will have a greater number of paths to travel across a magnetoelectric composite, thus diminishing the **ME** effect.

We also observed that for spherical particles the inter-phase **H-E** coordination number (CNHE) associated with mechanical coupling between phases is likely to increase quadratically as the piezoelectric **E** phase particles deform during sintering. However, allowing the **E** phase particles to deform during sintering may counteract the **ME** enhancing effect of reducing **E**-phase relative particle size by lowering the percolation threshold. The simulation data suggest that the best way to raise the electrical percolation threshold ρ_c while maintaining a maximum mechanical coupling between the **E** and **H** phases is to use piezoelectric **E** particles at $(3.5)^{-1}$ the size of magnetostrictive **H** particles and promoting **E**-**H** particle affinity. Furthermore, during sintering it seems better to promote deformation of the **E** phase than deformation of the **H** phase in order to maximize mechanical coupling.

We also observed that the radius of gyration (**R$_g$**), which characterizes particle deformation, on average grows from **R$_g$** = 0.435 for perfectly spherical particles to an average value of **R$_g$** = 0.5925 in all cases for a fixed simulation time of 3800 time steps, with a narrow spread for the primary peak in Fig. 11. Therefore, not only do all simulations stop at less than 25% mass transport away from the center of mass of each cluster, but they also arrive at a precise relative increase in radius of gyration **R$_g$** of (0.5925-0.435/0.435) $\times$100 = 36.2%, for a fixed simulation run time of 3800 time steps, thus implying a relationship between sintering time and extent of particle deformation.

Regarding pre-sintering particle mixing, numerous studies including [41–44] report phase segregation when mixing particles of different sizes or mass, which is highly deleterious to the percolation threshold. Therefore, it is required that the **H** and **E** phases are well mixed prior to sintering,

as documented in [1]. In addition, we confirmed the results of [34,37] and others showing that the coordination number for random close packed hard-shell spheres is approximately between 5.9 and 6.7. Furthermore, we propose a simplified qualitative model that shows that the coordination number between bi-disperse spheres increases quadratically with a decrease in relative particles size (R_H/R_E) between the two species.

Acknowledgements

Compliance with ethical standards

Conflict of interest. On behalf of all authors, the corresponding author states that there is no conflict of interest resulting from this manuscript.

Appendix A. Programs used for hard-shell modeling

The following list illustrates the order in which the programs are to be run in order to produce the results reported in [1] for hard shells. All programs in this appendix were run on ASUS 2.53 GHz 64 bit Windows 7 Home Premium 2009. References [45,46] provide background for these programs. LAMMPS [22] was run on the West Virginia University High Performance Cluster under UNIX operating system. *All programs and scripts are provided as supplementary material in the publisher's website.*

Program	Purpose
1. pmpe4.c	Produce set of input coordinates for Lammps for R_H/R_E=4.
2. Lammps_LT_MIX.txt	Run Lammps. See appendix C for MIX script
3. cvt_dmp_inp2.pl	Convert output Lammps dump file to input data file.
4. Lammps_LT_EQU.txt	Run Lammps. See appendix C for EQU script
5. cvt_dmp_inp3.pl	Convert output dump file to input data file.
6. Lammps_LT_GEL.txt	Run Lammps. See appendix C for GEL script
7. filt_coords_PM-2.pl	Strip unnecessary information from dump file.
8. filt_coords_PE-2.pl	Strip unnecessary information from dump file.
9. filt_coords_PM-R.pl	Strip unnecessary information from dump file.
10. dist3_Rm	Create file of bond pairs. Rm= connection radius
11. zap2_Rm	Recurse through bond pairs and evaluate percolation.
12. CNHH_Rm	Calculate c.n. for all H particles with respect to other H particles.
13. pa64	Calculate local packing fraction

Appendix B. Programs used for particle deformation

The following list represents the order in which the programs in this appendix are to be run to produce the results for deformable H and E phase particles simulations reported in this paper. All programs in this appendix were run on a model ASUS 2.53 GHZ running 64 bit Windows 7 Home Premium 2009. References [45,46] provide background for these programs. LAMMPS [22] was run on the West Virginia University High Performance Cluster running a UNIX operating system. *All programs and scripts are provided as supplementary materials in the publisher's website.*

Program	Purpose
1. filt_coords_PM-2.pl	Strip unnecessary information from data file. See App. A.
2. filt_coords_PE-2.pl	Strip unnecessary information from data file. See App. A.
3. glob3_p	Replace all H coordinates with 125 point cubes, where p is the packing fraction defined as p= N_H / (N_H+N_E)
4. Lammps_LT_input_MIX7.txt	Run Lammps. See MIX7 script in Appendix C.
5. Lammps_LT_input_redump.txt	Remove all but coordinates from single timestep.
6. filt_coords_PM-mol-R.pl	Strip away unnecessary information from data file.
7. filt_coords_PE-mol.pl	Strip away unnecessary information from data file.
8. Rg3.pl_ts_p	Compute table of $\mathbf{R_g}$ values for each cluster.
9. dist9M_p	Create file of bond pairs between molecules
10. ZapM_p	Recurse through bond pairs and test for percolation
11. CNHH-M	Compute c.n. between H phase clusters
12. CNHE-M	Compute c.n. between H and E hard-shell spheres

Appendix C. Lammps scripts

The following are input scripts used by Lammps [22] for this study. The scripts need to be adjusted and customized depending on particles size and volume fraction of particles. *All programs and scripts are provided as supplementary materials in the publisher's website.*

Script	Purpose
1. RUNS8_MIX_R11_B [1].	MIX stage for Noa and Adh conditions for hard-shell spheres
2. RUNS7_R11_Adh_B64	EQU stage under Noa conditions for hard-shell spheres [1].
3. RUNS7_R11_NoA_B64	GEL stage under Noa conditions for hard-shell spheres [1].
4. MIX7_SNT_GLOB_G16	Simulate sintering under A00 and Noa conditions involving particle deformation (this paper).

Antoine Joseph Bedard Jr. and Ever J. Barbero. Electrical percolation threshold of magnetostrictive inclusions in a piezoelectric matrix under simulated sintering conditions. Computational Particle Mechanics (2018) 5:593-605. DOI: 10.1007/s40571-018-0192-9

Bibliography

[1] E.J. Barbero, A.J. Bedard, Electrical percolation threshold of magnetostrictive inclusions in a piezoelectric matrix composite as a function of relative particle size, Comput. Part. Mech. (2018) 5(2) 227–238. doi:10.1007/s40571-017-0165-4.

[2] T.I. Muchenik, E.J. Barbero, Charge, voltage, and work-conversion formulas for magnetoelectric laminated composites, Smart Mater. Struct. 24 (2015) 025039 (15 pp.)-.

[3] T.I. Muchenik, E.J. Barbero, Prediction of extrinsic charge, voltage, and work-conversion factors for laminated magnetoelectric composites, Smart Mater. Struct. 25 (2016) 015006 (16 pp.)-.

[4] W. Eerenstein, N.D. Mathur, J.F. Scott, Multiferroic and magnetoelectric materials, Nature. 442 (2006) 759–65.

[5] R. Grossinger, G.V. Duong, R. Sato-Turtelli, The physics of magnetoelectric composites, J. Magn. Magn. Mater. 320 (2008) 1972–7.

[6] J. Ma, J. Hu, Z. Li, C.-W. Nan, Recent progress in multiferroic magnetoelectric composites: From bulk to thin films, Adv. Mater. 23 (2011) 1062–1087.

[7] C.-W. Nan, M.I. Bichurin, S. Dong, D. Viehland, G. Srinivasan, Multiferroic magnetoelectric composites: Historical perspective, status, and future directions, J. Appl. Phys. 103 (2008). http://dx.doi.org/10.1063/1.2836410.

[8] M. Bichurin, V. Petrov, S. Priya, A. Bhalla, Multiferroic Magnetoelectric Composites and Their Applications, Adv. Condens. Matter Phys. 2012 (2012) 129794.

[9] J.K. Mackenzie, R. Shuttleworth, A phenomenological theory of sintering, Proc. Phys. Soc. B. 62 (1949) 833–852.

[10] C. Herring, Effect of change of scale in sintering phenomena, J Appl. Phys. 21 (n.d.) 301.

[11] R. Bjork, V. Tikare, H.L. Frandsen, N. Pryds, The sintering behavior of close-packed spheres, Scr. Mater. 67 (2012) 81–84.

[12] W. Zhang, R.E. Eitel, Low-temperature sintering and properties of 0.98PZT-0.02SKN ceramics with LiBiO2 and CuO addition, J. Am. Ceram. Soc. 94 (2011) 3386–3390.

[13] X. Chao, D. Ma, R. Gu, Z. Yang, Effects of CuO addition on the electrical responses of the low-temperature sintered Pb(Zr0.52Ti0.48)O3-Pb(Mg1/3Nb2/3)O3-Pb(Zn1/3Nb2/3)O3 ceramics, J. Alloys Compd. 491 (2010) 698–702.

[14] G. Srinivasan, E.T. Rasmussen, J. Gallegos, R. Srinivasan, Y.I. Bokhan, V.M. Laletin, Magnetoelectric bilayer and multilayer structures of magnetostrictive and piezoelectric oxides, Phys. Rev. B Condens. Matter Mater. Phys. 64 (2001) 214408–1.

[15] R. Orru, R. Licheri, A.M. Locci, A. Cincotti, G. Cao, Consolidation/synthesis of materials by electric current activated/assisted sintering, Mater. Sci. Amp Eng. R Rep. 63 (2009) 127–287.

[16] L. Weng, Y. Fu, S. Song, J. Tang, J. Li, Synthesis of lead zirconate titanate-cobalt ferrite magnetoelectric particulate composites via an ethylenediaminetetraacetic acid-citrate gel process, Scr. Mater. 56 (2007) 465–468.

[17] K.M. Allen, N. Auyeung, N. Rahmatian, J.F. Klausner, E.N. Coker, Cobalt Ferrite in YSZ for Use as Reactive Material in Solar Thermochemical Water and Carbon Dioxide Splitting, Part II: Kinetic Modeling, JOM. 65 (2013) 1682–93.

[18] S. Hara, A. Ohi, N. Shikazono, Sintering analysis of sub-micron-sized nickel powders: kinetic Monte Carlo simulation verified by FIB-SEM reconstruction, J. Power Sources. 276 (2015) 105–12.

[19] A. Bunde, W. Dieterich, Percolation in composites, J. Electroceramics. 5 (2000) 81–92.

[20] C.-W. Nan, Y. Shen, J. Ma, Physical Properties of Composites near Percolation, Annu. Rev. Mater. Res. 40 (2010) 131–51.

[21] E.J. Barbero, Multifunctional Composites, first edition, CreateSpace Independent Publishing, South Charleston, SC (2015).

[22] S. Plimpton, Fast parallel algorithms for short-range molecular dynamics, J. Comput. Phys. 117 (1995) 1–19.

[23] A. Donev, S. Torquato, F.H. Stillinger, R. Connelly, Jamming in hard sphere and disk packings, J. Appl. Phys. 95 (2004) 989–99.

[24] A.R. Kansal, S. Torquato, F.H. Stillinger, Computer generation of dense polydisperse sphere packings, J. Chem. Phys. 117 (2002) 8212–18.

[25] E. Zaccarelli, S.V. Buldyrev, E. La Nave, A.J. Moreno, I. Saika-Voivod, F. Sciortino, P. Tartaglia, Model for reversible colloidal gelation, Phys. Rev. Lett. 94 (2005) 218301–1.

[26] L.C. DeJonghe, M.N. Rahaman, Chapter 4. Sintering of Ceramics, in: Handb. Adv. Ceram. Mater. Appl. Process. Prop., Academic Press, 2003.

[27] I.S. Beloborodov, A.V. Lopatin, V.M. Vinokur, Coulomb effects and hopping transport in granular metals, Phys. Rev. B Condens. Matter Mater. Phys. 72 (2005) 125121–1.

[28] D. Carrera, Quantum Tunneling in Chemical Reactions, (2007). https://www.princeton.edu/chemistry/macmillan/group-meetings/DEC_tunneling.pdf (accessed December 25, 2017).

[29] S. Kadkhodazadeh, J.B. Wagner, H. Kneipp, K. Kneipp, Coexistence of classical and quantum plasmonics in large plasmonic structures with subnanometer gaps, Appl. Phys. Lett. 103 (2013) 083103 (4 pp.)-.

[30] M.D. Rintoul, S. Torquato, Computer simulations of dense hard-sphere systems, J. Chem. Phys. 105 (1996) 9258–65.

[31] P. Jalali, M. Li, An estimate of random close packing density in monodisperse hard spheres, J. Chem. Phys. 120 (2004) 1138–9.

[32] J. Kim, J. Li, Percolation threshold of conducting polymer composites containing 3D randomly distributed graphite nanoplatelets, Compos. Sci. Technol. 67 (2007) 2114–20.

[33] Radius of gyration, Wikipedia. (2017). https://en.wikipedia.org/w/index.php?title=Radius_of_gyration&oldid=814930481 (accessed December 26, 2017).

[34] A. Bezrukov, M. Bargiel, D. Stoyan, Statistical analysis of simulated random packings of spheres, Part. Part. Syst. Charact. 19 (2002) 111–118.

[35] G.S. Rohrer, Structure and Bonding in Crystalline Materials, 1 edition, Cambridge University Press, Cambridge ; New York, 2001.

[36] S.S. Tulluri, Analysis of Random Packing of Uniform Spheres Using the Monte Carlo Simulation Method, New Jersey Institute of Technology, Department of Mechanical Engineering, 2003.

[37] J. Zhou, Y. Zhang, J.K. Chen, Numerical simulation of random packing of spherical particles for powder-based additive manufacturing, J. Manuf. Sci. Eng. 131 (2009) 031004 (8 pp.)-.

[38] P. Richard, L. Oger, J.P. Troadec, A. Gervois, A model of binary assemblies of spheres, Eur. Phys. J. E. 6 (2001) 295–303.

[39] H. Scher, R. Zallen, Critical density in percolation processes, J. Chem. Phys. 53 (1970) 3759–61.

[40] H. Liang, W. Wang, Coordination numbers for rigid spheres and local compositions, Fluid Phase Equilibria. 24 (1985) 165–75.

[41] J.M. Ottino, D.V. Khakhar, Mixing and segregation of granular materials, Annu. Rev. Fluid Mech. 32 (2000) 55–91.

[42] S.W. Meier, R.M. Lueptow, J.M. Ottino, A dynamical systems approach to mixing and segregation of granular materials in tumblers, Adv. Phys. 56 (2007) 757–827.

Antoine Joseph Bedard Jr. and Ever J. Barbero. Electrical percolation threshold of magnetostrictive inclusions in a piezoelectric matrix under simulated sintering conditions. Computational Particle Mechanics (2018) 5:593-605. DOI: 10.1007/s40571-018-0192-9

[43] D.C. Rapaport, Molecular dynamics simulation: a tool for exploration and discovery using simple models, J. Phys. Condens. Matter. 26 (2014) 503104 (18 pp.)-.

[44] K. van der Vaart, P. Gajjar, G. Epely-Chauvin, N. Andreini, J.M.N.T. Gray, C. Ancey, Underlying Asymmetry within Particle Size Segregation, Phys. Rev. Lett. 114 (2015) 238001 (5 pp.)-.

[45] D. Stauffer, A. Aharony, Introduction to Percolation Theory: Revised Second Edition, 2 edition, Taylor & Francis, London, 1994.

[46] Kruse, Data Structures & Program Design 3rd Ed, Prentice Hall of India, New Delhi, 2007.